Advanced Materials

ADVANCED MATERIALS
www.advmat.de

RESEARCH ARTICLE

A Radial Modulus-Gradient Fiber for Chronic Recording and Decoding in Deep Brain

Liyuan Wang[1] | Chengqiang Tang[1] | Zhengqi Han[2] | Haixin Zhong[3] | Kailin Zhang[1] | Ziyi Xie[4] | Hang Guan[1] | Peng Zhai[5] | Hongjian Li[2] | Jiaheng Liang[2] | Jiajia Wang[1] | Jiawei Chen[1] | Yiqing Yang[1] | Ziwei Liu[1] | Mingyi Huang[3] | Sihui Yu[1] | Qingquan Han[1] | Xiangran Cheng[1] | Jinyan Li[1] | Jiahao Shen[6] | Xiaofei Wang[6] | Cheng Cao[6] | Biqin Dong[7] | Lihua Zhang[5] | Qi Tong[6] | Chen Zhao[1] | Ya Huang[1] | Bingjie Wang[1] | Songlin Zhang[1] | Peining Chen[1] | Jue Deng[4] | Yuguo Yu[3] | Hongbo Yu[2] | Huisheng Peng[1] | Xuemei Sun[1]

[1]State Key Laboratory of Molecular Engineering of Polymers, Department of Macromolecular Science, Institute of Fiber Materials and Devices, and Laboratory of Advanced Materials, Fudan University, Shanghai, China | [2]School of Life Sciences, State Key Laboratory of Brain Function and Disorders, Fudan University, Shanghai, China | [3]Research Institute of Intelligent Complex Systems, State Key Laboratory of Medical Neurobiology and MOE Frontiers Center for Brain Science, Institutes of Brain Science, Institute of Science and Technology for Brain-Inspired Intelligence, Artificial Intelligence Laboratory, Fudan University, Shanghai, China | [4]College of Biomedical Engineering, Fudan University, Shanghai, China | [5]The Institute of AI and Robotics, Fudan University, Shanghai, China | [6]Department of Aeronautics and Astronautics, Fudan University, Shanghai, China | [7]College of Biomedical Engineering, Yiwu Research Institute, Fudan University, Shanghai, China

Correspondence: Jue Deng (dengj@fudan.edu.cn) | Yuguo Yu (yuyuguo@fudan.edu.cn) | Hongbo Yu (hongboyu@fudan.edu.cn) | Huisheng Peng (penghs@fudan.edu.cn) | Xuemei Sun (sunxm@fudan.edu.cn)

Received: 7 October 2025 | **Revised:** 4 February 2026 | **Accepted:** 10 April 2026

Keywords: carbon nanotube fiber | fiber devices | gradient-modulus | hydrogel | neural recordings

ABSTRACT

Fiber electronics provide the most promising platform for the detection, modulation, and reconstruction of biosignals in the brain. However, preserving stable communication between fiber electronics and cellular-scale targets in the deep brain is critical but challenging because of their mechanical mismatch. Here, our study fills this gap by developing a radial modulus-gradient fiber (RMGF), which can bridge high-modulus conductive components (MPa) and low-modulus brain tissue (kPa) to well eliminate the mechanical mismatch at the entire neural–device interface. The RMGF exhibits strain-insensitive electrical properties (<0.2% resistance fluctuation over 700,000 stretching–release cycles). As an example, the RMGF enables unprecedented five-month continuous tracking of single neurons in the dorsal lateral geniculate nucleus of freely moving cats, and allows reconstruction of visual stimuli with the use of only three neurons, with a high correlation coefficient of 0.95, approaching the theoretical limit of the unscented Kalman filter (0.97). The results indicate that dorsal lateral geniculate nucleus neurons maintain stable tuning properties (spatial frequency sensitivity, ON/OFF characteristics, and X-cell classification) and reveal a minimal effective ensemble for efficient encoding of information within deep thalamic circuits. This RMGF represents a platform for chronic recording at the single-cell level and investigating fundamental mechanisms in the deep tissues.

Liyuan Wang, Chengqiang Tang, Zhengqi Han, Haixin Zhong and Kailin Zhang contributed equally to this work.

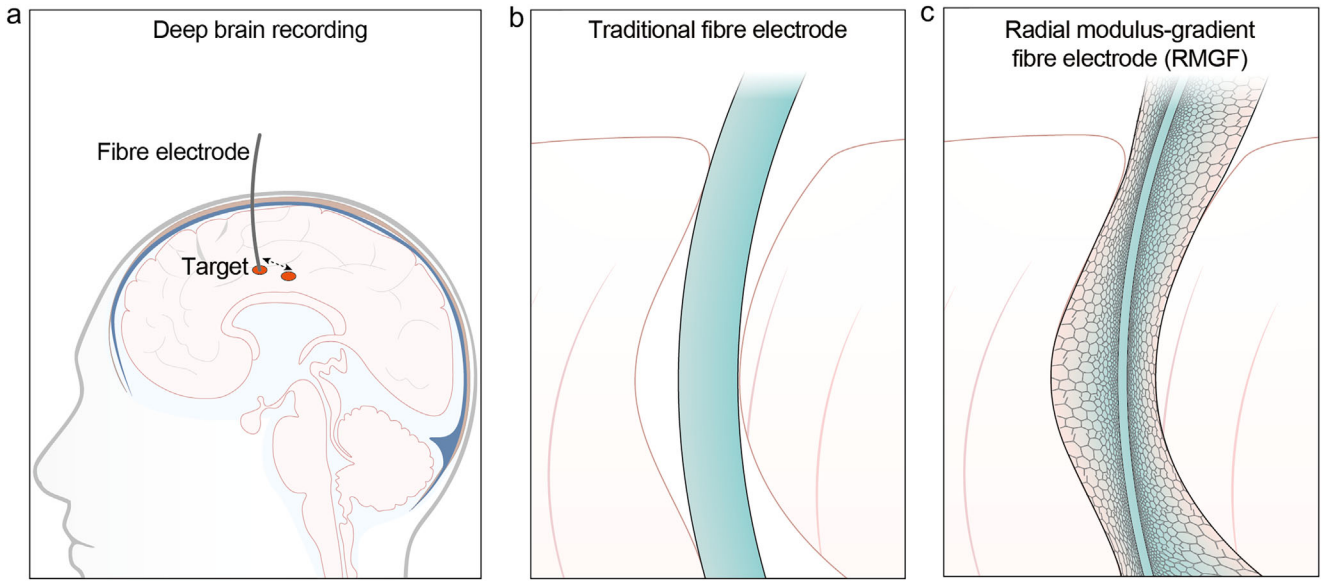

FIGURE 1 | Design and concept of the radial modulus-gradient fiber electrode (RMGF). (a) Schematic illustration of a fiber electrode tracking a small target within the dynamic deep brain. (b) The electrode–brain interface of a traditional fiber electrode implanted in the dynamic brain is disrupted, resulting in stress concentration and a discontinuous interface with the surrounding brain. (c) The RMGF establishes a stable and continuous interface with the dynamic brain.

1 | Introduction

Unveiling the mysteries of the brain has long been a dream of humanity. In the whole brain, deep brain regions play a central role in regulating essential functions [1–4]. Acquiring high-fidelity electrical signals from individual neurons within such deep regions is fundamental to advancing our understanding of brain function and its evolution. Fiber electronics have been recognized as the most promising tool for extracting electrical signals from brain tissue [5–8], owing to their ability to form intimate contact with the cellular-scale targets in deep (Figure 1a). However, it remains a challenge for traditional fiber electronics to stably and continuously track and record single-neuron activity within the deep brain over prolonged periods [9, 10]. The main difficulty arises from the inherent three-dimensional motion of soft brain tissues induced by routine activities; even breathing alone can cause persistent millimeter-scale shifts in neuronal positions [11–13].

Despite decades of development, the design of fiber electronics has remained unchanged. These fiber electronics are typically constructed from relatively high-modulus and non-stretchable metals or carbon-based electrodes and demonstrated a mechanically and structurally homogeneous configuration [14–18]. These devices cannot accommodate the several orders of magnitude softer brain tissue and maintain consistent electrical performance. Although some neural electrodes have been encapsulated with soft materials to mitigate this mechanical mismatch, they remain non-stretchable [19] and thus often lead to loss of close contact with target neurons in such dynamically deforming brain environments (Figure 1b). This issue has restricted consistent recording of neuronal activities for the assessment of neural messages encoded in individual neurons and their interactions. For example, while recent neural probes have enabled chronic recordings in small animals like mice and rats [14, 16, 18, 19], long-term recordings in the deep brain of large animals remain challenging, and are often compromised by signal drift, electrode fracture, and chronic inflammation. For example, state-of-the-art Neuropixels probes have primarily been used for acute recording at depths of less than ~1 cm below the cortex [20]. Consequently, chronic single-neuron recordings in the dorsal lateral geniculate nucleus (dLGN) of cat are rarely reported, due to its depth (~14 mm below the cortex), small size (~2 mm), and dynamic mechanical environment, further hindering our understanding of visual circuits and their underlying coding mechanisms.

Here, we overcome these limitations by designing a radial modulus-gradient fiber (RMGF) that can seamlessly and chronically track single neurons in deep brain regions. This RMGF consists of a spring multichannel electrode encased in a radial gradient hydrogel (Figure 1c). The radial modulus-gradient hydrogel with a well-tuned Young's modulus continuously bridges the mechanical disparity between high-modulus (megapascal level) conductive components and low-modulus (kilopascal level) brain tissues, forming an adaptive electrode–brain interface. The highly stretchable and reversible spring electrode accommodates axial tissue deformation while maintaining strain-insensitive electrical performance. Finite element analyses and two-photon imaging further validate the robust integration of the RMGF with three-dimensional deforming brain tissue without stress concentration or device dislocation, both theoretically and experimentally. We further demonstrate the chronic functionalities of the RMGF in the deep brain of cats. For example, the RMGF can be implanted into the dLGN of freely moving cats for stable and continuous recording of single-neuron electrophysiological signals and identification of the visual function of individual neurons over 5 months. Without the loss of original signals or misrecording of signals from adjacent neurons that often occur with traditional fiber electronics, high-precision in situ reconstruction of visual information is achieved with a correlation coefficient of 0.95,

approaching the theoretical limit of 0.97. This advancement further facilitates novel investigations of super-sparse coding mechanisms, in which only three dLGN neurons are found to be sufficient to reconstruct the temporal dynamics of a visual stimulus. Finally, scalable and standardized manufacturing could be applied to obtain diverse fiber bioelectronics with the proposed configuration, offering widely applicable tools for biomedical applications.

2 | Results and Discussion

2.1 | Design Principles and Characterization of the RMGF

The native tendon exhibits gradients in both structure and mechanical performance, enabling stable integration between the soft muscle and rigid bone [21–23]. Inspired by this principle, a gradient architecture was designed to provide mechanical properties that vary across the radial axis of the fiber, enabling a stable interface and gradual mechanical transition between high-modulus conductive components and low-modulus brain tissue. However, fabricating such gradient structures with a steep modulus transition from MPa to kPa levels within a short radial distance of ten to several hundreds of micrometers remains challenging. Existing gradient hydrogel fabrication strategies [24–26], such as layer-by-layer assembly, 3D printing, microfluidics, fluid mixing, and electro-based methods, generally suffer from discontinuous gradients, limited spatial resolution, complex processing, or restricted material compatibility, particularly when applied in a thin fiber. The electric field can be precisely tuned through parameters such as the voltage, pulse waveform, duration, and cycle number. Utilization of the electrothermal effect of conductive components is a promising strategy for accurately generating gradient temperature fields. Polyvinyl alcohol (PVA) hydrogels exhibit unique advantages due to their intrinsic similarities to biological tissues, including high water content, tissue-like mechanical softness and high biofunctionality [27, 28]. Also, PVA hydrogel can be physically crosslinked through freeze-thaw cycling, avoiding chemical crosslinkers and thereby offering enhanced biocompatibility over traditional chemically crosslinked hydrogels [29]. Their crystallinity can also be well-tuned by adjusting the temperature. Thus, we invented a two-step strategy that transforms a homogenous structure into a desired gradient by using an electrically induced temperature gradient to create a crystallization gradient in PVA. Initially, a homogeneous hydrogel was prepared around a conductive electrode by gelatinizing a precursor solution of PVA and sodium alginate. Subsequently, electrical pulses were applied to generate a radial thermal gradient around the conductive electrode. This process induced differential crystallization of PVA at various temperatures, transforming the initially uniform structure into a radial gradient from the inner to outer regions (Figure 2a). Microscopic imaging confirmed the structural integrity of the RMGF (Figure 2b). Both confocal microscopy and scanning electron microscopy (SEM) images revealed a radial gradient in the porosity, with the pore size progressively increasing from approximately 500 nm near the electrode core to approximately 8 μm at the outer boundary (Figure 2c,d). Raman spectroscopy mapping further confirmed the presence of a radial crystallization gradient, as indicated by the ratio of the intensity of the crystalline peak of PVA at 1140 cm^{-1} to that of the amorphous peak of PVA at 1090 cm^{-1}, which decreased from inside to outside [30] (Figure 2e). Together, this systematic structural characterization verified the formation of a radial gradient.

High temperatures induced high crystallization of PVA [31], resulting in a high local modulus. Therefore, we validated the gradient modulus of the RMGF, which had a high modulus near the rigid conductive components and a low modulus toward the outer soft biological tissues (Figure 2f,g). In addition, the gradient thermal field could be rationally controlled to vary the gradient modulus to match the Young's modulus of different electrode materials and surrounding biological tissues. The amplitude and width of the electrical pulses were adjusted to induce different modulus gradients. As the pulse amplitude was changed from 0.05 to 0.09 A, corresponding to a maximum temperature rise from 40°C to 90°C, the Young's modulus of the inner hydrogel sheath increased from 1.0 to 2.9 MPa (Figure 2f). The Young's modulus outside the hydrogel sheath decreased from 1.2 MPa to 200 kPa when the pulse width was changed from 5 to 0.5 s (Figure 2g). By systematically tuning the fabrication parameters, a Young's modulus ratio of 0.03–0.1 between the superficial and deep hydrogel layers was achieved. Overall, these strategies enable the radial modulus-gradient hydrogel to mechanically match various electrodes, including polymer, silk, or carbon-based electrodes, while closely aligning with the mechanical properties of soft biological tissues such as muscle, skin, and brain (Figure 2h).

To capture weak single-neuron-level bioelectrical signals in soft and dynamic deep brain tissue, the conductive component must be mechanically stretchable while maintaining stable resistance during repeated deformation. Traditional methods, such as depositing metal layers on stretchable substrates or embedding conductive fillers into elastomers, often suffer from degradation of the conductive layer/network during deformation, resulting in reduced electrical performance. Moreover, the insulating layers commonly used in vivo lack stretchability, further complicating the development of stretchable electrodes. Spring structures, which are inherently stretchable through geometric deformation rather than intrinsic material strain, are compatible with both stretchable and nonstretchable materials. Importantly, spring electrodes fabricated by twisting conductive fibers retain reversible electrical conductivity and structural integrity during repeated stretching–release cycles, enabling them to accommodate three-dimensional tissue deformations while maintaining stable electrical properties. Given that a small diameter is beneficial for minimizing tissue damage and recording single-neuron signals, finite element simulations were conducted to compare the diameter expansion ratios among different conductive materials. Owing to the aligned arrangement of nanoscale interspaces among carbon nanotube (CNT) fibers, allowing torsional deformation, CNT fibers exhibited a minimum diameter expansion of only 1.85 (Figure S1). Thus, CNT fibers coated with a thin insulating layer of parylene C were chosen for fabricating the spring electrode (Figure S2). Although thermal treatment was involved during gradient hydrogel fabrication, the near-zero thermal expansion of CNT fibers minimized thermally induced strain [32, 33], resulting in negligible thermal stress on the parylene C layer. Parylene C itself also exhibited low thermal expansion [34], and any residual strain could be further dissipated through

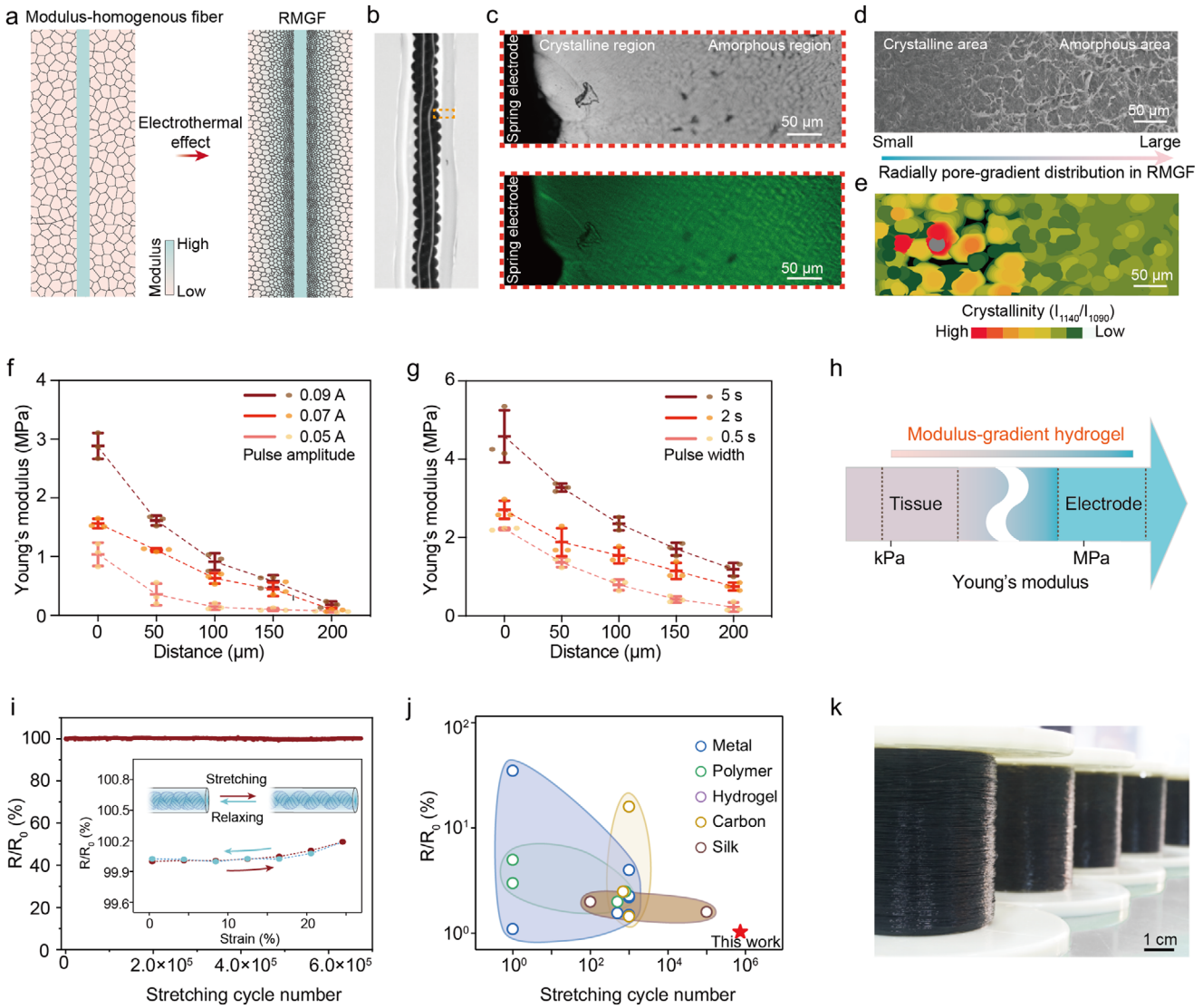

FIGURE 2 | Characterization of RMGFs. (a) Formation of an RMGF from a modulus-homogeneous fiber via the electrothermal effect. (b) Microscope image of the RMGF. (c,d) Representative bright-field (top in c), fluorescence (bottom in c) confocal images, and cross-sectional SEM image (d) showing the radial gradient structure in the RMGF, with smaller pores in the crystalline region and larger pores in the amorphous region. (e) Raman mapping image showing the radial gradient distribution of crystallinity in the RMGF, with a crystalline region near the spring electrode and an amorphous region farther away. (f,g) Gradient distributed Young's modulus in the RMGF from the inner core to the outer surface, modulated by the pulse amplitude (f) and pulse width (g). The data are presented as the mean ± s.d. (h) Modulus-gradient hydrogel bridging the gap between various soft tissues and conventional rigid electrode materials. (i) The resistance of the RMGF remained stable after 700,000 stretching cycles at 25% strain. The insert plot shows the resistance of the RMGF returning to its initial value after a stretching–relaxation cycle, with fluctuations of ± 0.2%. (j) Comparison of the electrical stability between previously reported electrodes and our RMGF under repeated deformation. (k) Scalable production of RMGFs.

internal CNTs sliding and the outer hydrogel layer with kPa-level modulus. Consistent with this analysis, SEM characterization confirmed that no tearing of the Parylene C layer occurred after gradient formation (Figure S3). The experiment involving the extraction of the RMGF from an electrolyte further revealed that the device resistance remained stable (Figure S4). Together, these results indicated that the insulating layer maintained high structural stability during the formation of the spring electrode and gradient hydrogel, effectively shielding the device side from external signal interference.

Owing to the spring structure and the highly reversible conductive network of CNT fibers, the resulting RMGF showed high stretchability, with strains of more than 150% (Figure S5) and strain-insensitive electrical performance. The RMGF had a high electrical conductivity of 10^5 S/m and a resistance change of less than 0.2% under 25% tensile strain over 700,000 stretching–release cycles (Figure 2i). Both the resistance stability and durability significantly exceeded those of previously reported stretchable electrodes (Figure 2j; Table S1), showing the potential for chronic applications in dynamically deformed biological tissue. In addition, the electrical performance, including the resistance and impedance, of the RMGF remained stable during repeated stretching at deformation frequencies ranging from 0.1 to 10 Hz (Figure S6), which is consistent with the dynamic frequencies of many biological tissues. The impedance of the RMGF

remained stable under dynamic stretching conditions (Figure S7). Furthermore, the electrical resistance of 3-cm-long RMGFs remained above 95% of the initial value under compressive loads ranging from 50 to 50,000 N and various curvature radii, even fully folded. Furthermore, less than 5% resistance variations were observed after 5000 bending cycles at a curvature radius of 5 mm (Figure S8), ensuring reliable electrical communication during tissue deformation.

2.2 | Scalable Fabrication of RMGFs

Additionally, to verify the universality of the RMGF construction strategy, standardized and scalable production through systematic variation of key structural parameters was demonstrated (Figure S9a–d). Specifically, this fabrication strategy showed broad applicability, enabling gradient hydrogel structures to be integrated onto various fiber electrodes, including CNT fibers and metal wires (Figure S9e). Multichannel electrode configurations could be achieved by adjusting the number of conductive fibers (Figure S9f,g). The hydrogel coating thickness could be precisely controlled by modulating the extrusion speed, while the gradient distribution within the hydrogel could be finely tuned by varying the pulse parameters. The resulting RMGFs could be obtained in highly consistent rolls, tailored to specific lengths and integrated with a wireless recording system for biomedical applications in vivo (Figure S10).

2.3 | Theoretical and Experimental Demonstrations of the Deformation Adaptation of the RMGF

To theoretically evaluate the ability of the RMGF to promote integrality and stability in soft tissues under dynamic deformation, finite element analyses were employed to investigate the effect of the gradient hydrogel on the stress distribution at the electrode–tissue interface (Figure S11 and Table S2). The simulation results revealed that the gradient hydrogel effectively dissipated the stress concentration, ensuring a smooth mechanical transition from the surrounding tissue to the electrode (Figure 3a). In contrast, a fiber electrode coated with a homogeneously high-modulus hydrogel (MPa level) induces stress at the hydrogel/tissue interface, easily causing damage to the surrounding brain. A homogeneously low-modulus hydrogel (kPa level) creates obvious stress concentration at the electrode/hydrogel interface (Figure 3b), potentially leading to interfacial delamination, tearing and fatigue of hydrogel layers under repeated deformation. The effects of the hydrogel thickness and modulus gradient on the stress distribution were further investigated. The stress concentration was effectively alleviated, and the peak stress position shifted from the electrode/hydrogel interface to the interior of the gradient hydrogel while the peak stress value decreased as the thickness increased (Figure 3b). Furthermore, stress concentration occurred at the electrode/hydrogel interface when the high modulus end of the gradient hydrogel was lower than that of the electrode, but this issue could be mitigated by increasing the modulus of the hydrogel. Similarly, the same rule could be applied to the low modulus end (Figure 3c). These findings further highlight the importance of controllable RMGF gradients.

To further experimentally validate these results, RMGFs were implanted into mouse brain tissue to observe changes in electrophysiological signals and the relative positions of RMGF tips and targets in brain tissue after deformation (Figure 3d). For each implanted electrode, six neuronal cell bodies or axons were selected as reference points (orange arrows in Figure 3g). The distances between these six reference neurons and the electrode tips were measured to assess positional integrality and stability under compression induced by the application of an external force on the brain tissue surface. All the groups share the same direction and magnitude of this external force. Through a systematic comparison of neural signal recordings between RMGFs and a commercial neural probe, the electrophysiological results demonstrated that both the waveform amplitude and full-width at half-maximum of the neuronal signals detected by the RMGFs remained stable before and after deformation (Figure S12). In contrast, the commercial neural probe exhibited signal loss after deformation (Figure 3e,f). Moreover, the relative distances between the RMGFs and surrounding reference neurons ($n = 6$ per electrode) remained almost unchanged, with a maximum change of less than 10%, whereas the commercial neural probe showed a relative distance change of more than 300% (Figure 3g,h). Furthermore, various stresses, including stretching and shaking, were applied to simulate the complex 3D deformation of the brain. No obvious changes were observed in the distance between reference neurons and electrode tips, as well as in the recorded amplitude and electrophysiological signals (Figures S13–S15), indicating that the RMGFs could adapt to the complex 3D deformation and continuously track the same neuron after implantation.

Furthermore, a variety of fiber electrodes, i.e., a spring electrode, a spring electrode with a homogeneous hydrogel, and a CNT fiber with a gradient hydrogel, were implanted into the deep brain. For comparison with the RMGF, the CNT fiber with the same gradient hydrogel had the same thickness and mechanical performance. The RMGF exhibited stable interfacing with surrounding neurons, whereas the CNT fiber with the same gradient hydrogel underwent obvious displacement relative to the target neurons (Figure 3g,h), showing the necessity of a spring structure in the axial direction. Similarly, the bare spring electrode and the hybrid spring electrode with a homogeneous hydrogel (both of which had the same spring electrode as the RMGF) showed obvious displacements during tissue deformation. Therefore, the combination of the dynamic adaptability of the spring structure and the radial gradient hydrogel–tissue interface enables the RMGF electrode tip to stably capture deep, dynamic brain targets.

2.4 | Chronic Single-Neuron Visual Electrophysiology in a Cat dLGN Enabled by RMGFs

The dLGN, which is a key relay in visual circuits, features a unique channel-specific coding scheme and transmits visual information closely resembling the original input [35]. Single-neuron-level recording and decoding of the dLGN over extended timescales can deepen our understanding of visual processing and encoding mechanisms, thus advancing treatments for vision-related diseases and visual intelligence technologies [36]. However, chronic recording of the dLGN remains unrealized because of its deep subcortical location (12–14 mm below the cortex), small

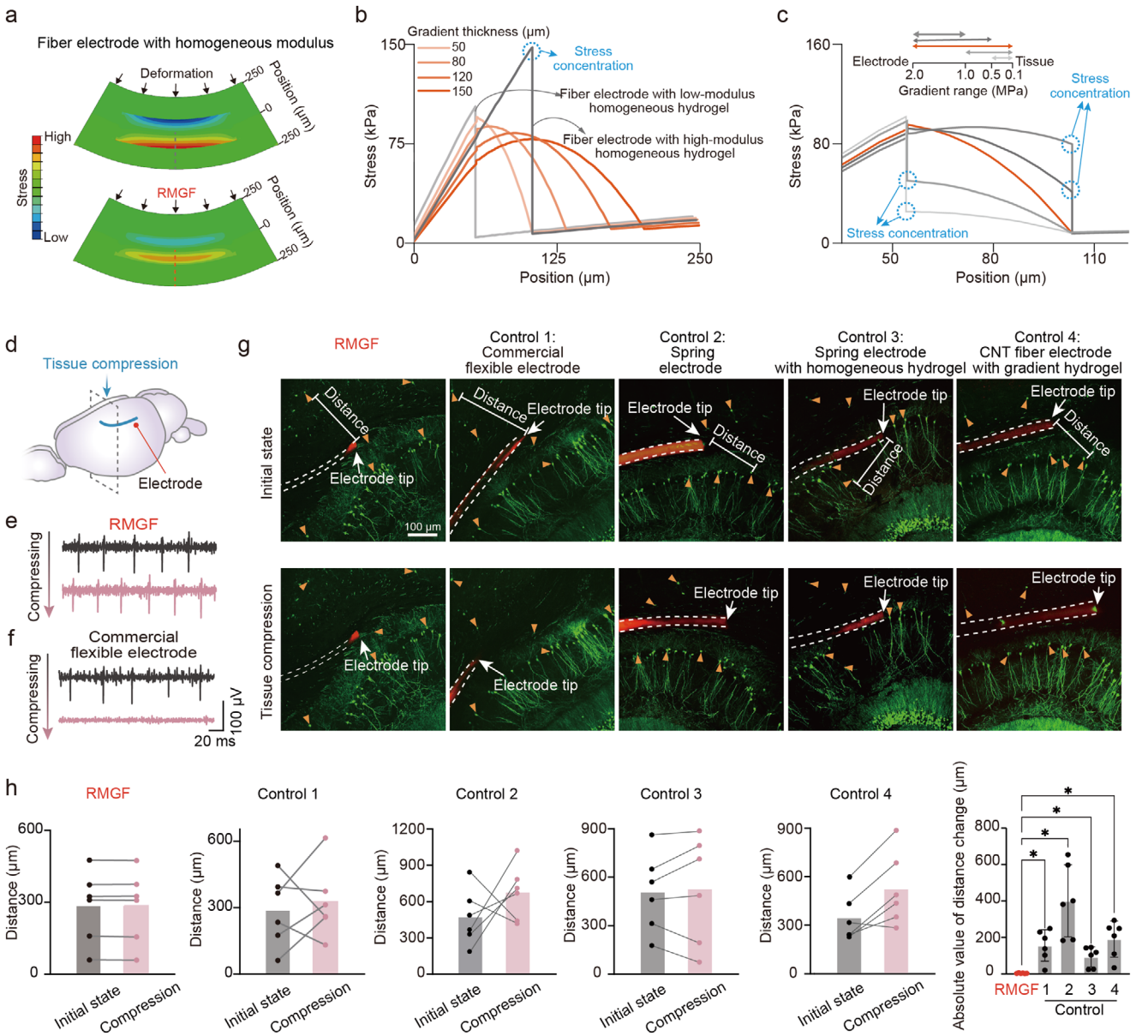

FIGURE 3 | Theoretical and experimental demonstrations of deformation adaptation of RMGFs. (a) Representative finite element analysis of a fiber electrode with modulus-homogeneous hydrogel (top panel) and an RMGF (bottom panel) under deformation, showing that less stress concentration occurred at the RMGF–brain interface. (b) Stress distributions along the central axis (dotted line in a) of RMGFs with different thicknesses of the gradient hydrogel. (c) Stress distributions along the central axis of RMGFs when the hydrogel has different modulus gradient ranges. (d) Schematic illustration of RMGF implantation in the mouse brain. (e,f) The electrophysiological signal detected by an RMGF remained stable, whereas the signal detected by a commercial flexible electrode was lost when the brain tissue was compressed. Initial state (dark line) and after compression (red line). (g) Representative two-photon fluorescence images of different electrodes implanted in brain tissues in the initial (top) and tissue compression (bottom) states. For each electrode, six surrounding neuronal cell bodies were selected as positional reference points (indicated by orange arrows). Scale bar, 200 μm. $n = 6$ biologically independent experiments for each group. (h) Changes in the distances between the electrode tip and six reference points per electrode in the initial state and after compression, showing that the RMGF can stably track the target under brain dynamic deformation. $n = 6$ biologically independent experiments for each group. The data in (h) are presented as the mean ± s.d.; significance is denoted as $^*p < 0.05$, two-tailed unpaired *t*-test.

size (~2 mm), multilayered structure, and substantial internal brain motion [37]. Leveraging the mechanical compliance and high-fidelity recording of the RMGFs, we implanted them into the dLGN of freely moving cats, which constitute a classical animal model for studying vision (Figure 4a).

We customized back-end circuits and connected them with RMGFs to obtain a neural recording system. The back-end circuits, including recording and wireless transmission modules, were fixed on the cat head, and an RMGF was implanted into the dLGN (Figure 4b,c). Since recordings of neurons vertically located in the dLGN are valuable for understanding visual circuits, we designed a 12-channel RMGF with all channels aligned along the axial direction to detect neurons in different layers of the dLGN. A continuous full-screen flash was presented to the cat, with both eyes alternately occluded or unoccluded

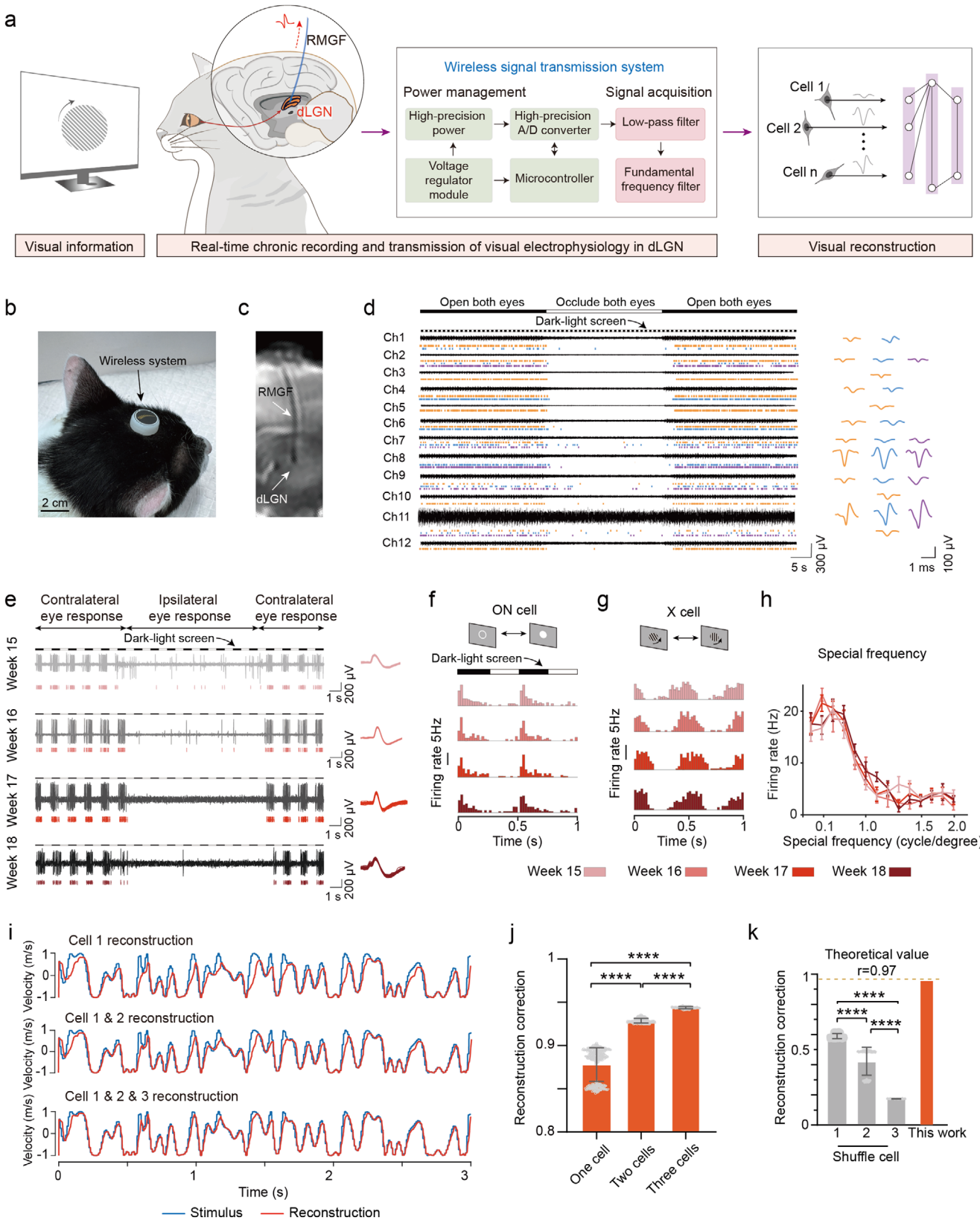

FIGURE 4 | Visual electrophysiology and reconstruction performed in the deep brain of cats enabled by RMGFs. (a) Schematic illustration showing the workflow of studying visual circuits by implanting RMGFs into the deep brain region (dLGN) of a freely moving cat. RMGFs capture single neuron signals and transmit them to a backup integrated wireless recording system. Finally, the recorded signals are used for visual reconstruction. (b) Representative image of an integrated wireless recording system, which can be mounted on the head of a cat, with RMGFs implanted into the dLGN. (c) MRI image showing the RMGF precisely implanted in the dLGN of a cat. (d) Representative fragments of neuronal activity (left) and corresponding waveforms of sorted spikes (right) in the dLGN recorded by multichannel RMGFs. $n = 3$ biologically independent experiments for each group. (e)

for 30 s. Nine of twelve channels in the RMGF responded significantly, with signal-to-noise ratios (SNR) exceeding 3, and several channels recorded spontaneous spikes even when both eyes were occluded. This allows accurate analysis of a series of specific visual reactive characteristics of the detected neurons (Figure 4d). Taking Channel 8 as an example, the detected neuron responded to light stimuli (classified as an ON cell) [38]. This neuron exhibited selective responsiveness to grating stimuli at a spatial frequency of 0.25 cycles per degree. Under rotating grating stimulation, it showed no orientation selectivity, and its firing pattern displayed sinusoidal modulation, consistent with the classification criteria of X cell [39]. Similarly, the visual reactive characteristics of the neurons detected by Channels 7 and 10 were successfully analyzed, with both being ON and X cells (Figure S16). Together, this RMGF can detect electrophysiological signals with a high SNR while enabling precise analysis of the visual reactive characteristics of target neurons.

Furthermore, in vivo chronic recording of single neurons was demonstrated by implanting RMGFs in the dLGN of cats. The RMGFs could maintain stable recording of a single neuron with a high SNR for 5 months, allowing accurate sorting of single-unit spikes (Figure 4e; Figure S17a). Further analyses, including high waveform similarity, stable autocorrelograms structure and inter-spike interval distributions, low within-week split-half variability, demonstrate that the same single neuron was reliably tracked using the RMGF (Figures S17 and S18). Owing to the high-fidelity recordings enabled by the RMGF, detailed and chronic analyses of their specific visual response characteristics in situ have been further achieved. For example, a tracked neuron with the characteristics of an ON cell was consistently excited by light stimuli (Figure 4f). Under continuously drifting grating stimuli, it acted as an X cell and showed no orientation sensitivity, with a spatial frequency of 0.35 cycles per degree (Figure 4g,h). The visual reactive characteristics of the target neuron remained consistent for 5 months, which has not been previously reported [40, 41]. This result may be due to the minimal relative displacement during continuous tracking of the neuron by the RMGF, thus maintaining a high SNR (> 5) without interference from other neurons. In contrast, commercial neural probes implanted in the dLGN exhibited a substantial loss of electrophysiological signals within two weeks (Figure S19). During the 5-month implantation in the brain, the immunofluorescence results revealed no obvious aggregation of glial cells around the RMGFs. Quantitative analysis further demonstrated that the fluorescence intensities of both GFAP and Iba1 around RMGF did not increase and remained comparable to those of the control group, indicating the high biocompatibility of the electrode in vivo (Figure S20). Furthermore, comparing with previously reported neural probes (Table S3), the results show that the RMGF enables stable single-neuron recordings at a deeper location in a medium-sized animal, supported by the gradient-modulus hydrogel and stretchable spring electrode. Taken together, these results indicate that the RMGF holds promise as a reliable tool for the chronic study of visual circuits and their related applications at the single-neuron level.

2.5 | High-accuracy Visual Reconstruction of a Cat dLGN by RMGFs

In situ visual decoding and reconstruction enable investigation of the response stability and plasticity of individual neurons or neuronal ensembles under different visual stimuli, offering insights into how the retina, dLGN, and visual cortex encode and process visual information. However, reliable decoding of the dLGN remains challenging, with current accuracies reaching only 0.52–0.79 [42]. We hypothesize that the precise and chronic recording capabilities of RMGFs will further enable high-accuracy visual decoding and reconstruction. Thus, a multichannel RMGF was used to continuously record multiple cells in the dLGN during drifting grating stimuli with a consistent 3 s pseudorandom velocity pattern across 100 trials (Figure 4i; Figure S21a), and the electrophysiology data of the detected cells were chosen to reconstruct the real-time pseudorandom velocity of drifting gratings by using the unscented Kalman filter. The reconstruction correlation, i.e., the ratio of the reconstructed and actual stimulus velocities of the drifting grating, was used to evaluate the accuracy of visual reconstruction.

Our visual reconstruction performance substantially improved with an increasing number of neurons (Figure 4i). Systematic analysis further revealed an obvious decrease in the response latency and a corresponding increase in mutual information as the number of neurons increased (Figure S21b–d). Unlike the classical neural coding theories that associate larger neuronal populations with higher decoding accuracy, we found that only 3 neurons achieved 0.95 accuracy in visual stimulus reconstruction (Figure 4i–k), approaching the theoretical limit (0.97) achievable with the unscented Kalman filter. The results validate that this small ensemble constitutes a “minimal effective ensemble” for super-sparse coding principles in deep brain circuits, supporting predictions of optimal minimal ensembles under low noise conditions. Moreover, these results are further supported by our computational modeling. In a biophysical spiking network of 300 excitatory and 75 inhibitory neurons, spike-timing-dependent plasticity self-organized a super-sparse code, with only 5.5 neurons (1.83%) responding strongly to any stimulus while maintaining high accuracy (Figure S22 and Table S4). This finding reveals that only a small number of neurons can efficiently encode visual information in deep thalamic circuits, differing from classical large-population assumptions in cortical regions

Recorded single-neuron activity over 5 months in response to light-dark stimuli under contralateral or ipsilateral eye opening. (f–h) Typical visual characteristics of the target neuron, including ON/OFF cells (f), X/Y cells (g), and special frequency (h). $n = 3$ biologically independent experiments for each group. (i,j) Neuronal response and reconstruction. (i) Original stimuli (blue), and reconstructed velocity (red). (j) Quantitative comparison of the stimulus–reconstruction correlation between the reconstructed and original stimuli for neuronal populations ranging from one to three cells. (k) Comparison of Pearson correlation coefficients from this work (0.95, stably tracking and recording 3 neurons) with the theoretical value (0.97) and shuffled data (randomly recording among 3 neurons in space). $n = 3$ biologically independent experiments for each group. The data in (j) and (k) are presented as the mean ± s.d.; significance is denoted as ****$p < 0.0001$, Two-sample Kolmogorov–Smirnov.

[43, 44]. To further verify that stable recordings by our RMGF are essential for high decoding fidelity, we artificially shuffled the neuronal recording order, which resulted in a marked decline in the decoding accuracy (Figure 4k). This result demonstrates that the high-accuracy visual reconstruction primarily benefits from the stable recordings enabled by the RMGF.

3 | Conclusion

We have made an RMGF for seamless interfacing with soft, dynamic biological tissue, enabling unprecedented chronic single-unit electrophysiological recording of small targets deep within the brain of a middle-sized animal model, which exhibits more vigorous movement than small-sized animals such as mice. Incorporating a stretchable spring conductive pathway and a modulus-gradient hydrogel sheath, the RMGF accommodates misalignment and mitigates the stress concentration at the interface between the rigid electrode and surrounding tissues. After implantation in the deep brain of cats, the RMGFs achieved 5-month stable single-neuron tracking with high-fidelity visual decoding (Pearson correlation coefficient of 0.95), approaching theoretical limits. This work not only provides the experimental validation of super-sparse coding evidence in deep brain structures, but also offers valuable blueprints for designing energy-efficient artificial systems capable of sustained, nondegrading performance. Building upon these strategies, a standardized and scalable production line for customized product fabrication was further established, paving the way for chronic sensing and modulation of small targets beyond tissue surfaces and offering a reliable tool for brain and other biomedical studies in vivo.

4 | Experimental Section

4.1 | Preparation of Radial Modulus-Gradient Fiber Electrode (RMGF)

Carbon nanotubes (CNTs) were synthesized using the floating catalyst chemical vapor deposition method [45]. The prepared CNT strips, approximately 1 mm in width, were twisted into CNT fibers with a diameter of approximately 8 μm. Parylene C was then deposited onto the surface of the CNT fibers as an insulation layer through a chemical vapor method (SCS PDS2010 Labcoter). The thickness of the insulation layer was approximately 3 μm. These CNT/Parylene C fibers were subsequently twisted into a spring configuration, forming single- or multiple-channel structures. The resulting spring was drawn out of a mixed hydrogel precursor (sodium alginate (A2033, medium viscosity, 0.5 wt.%); PVA (Mw = 146k–186k, 99+% hydrolyzed, 10 wt.%)) at a speed of 5 mm/s and immersed in a 5 wt.% calcium chloride solution. The resulting spring electrodes coated with a homogeneous hydrogel were dried at room temperature overnight. Subsequently, electrical pulses were applied to 10-cm-long spring electrodes to form a temperature gradient and the resulting modulus gradient of the hydrogel coating. The pulse parameters, including the pulse frequency, pulse amplitude, and cycle number, could be tuned to adjust the gradient moduli. After immersion in a saline solution, an RMGF was obtained. All chemicals were obtained from Sigma–Aldrich unless otherwise stated and were used without further purification. The structures of these fibers were characterized via scanning electron microscopy (SEM, Gemini SEM500, Zeiss) and confocal microscopy (EX51, Olympus).

4.2 | Mechanical Performance and Simulation of RMGFs

The stress–strain curves of the RMGFs were measured at a tensile rate of 10 mm/s using a tensile machine (HY0350). ABAQUS was further used to analyze the stress distributions for spring electrodes with modulus-homogeneous or modulus-gradient hydrogels. D_c represents the diameter of the core electrode, D_h represents the diameter of the whole electrode, L_h represents the length of the whole electrode, L_b represents the width, and Ls represents the length of the substrate tissue. The Young's moduli of the three hydrogel coatings were set as follows: homogeneous modulus (2.0 or 0.1 MPa) and gradient modulus with a high modulus (2.0 MPa) near the core and a low modulus (0.1 MPa) in the outer layer. The Young's moduli of the spring electrode core and substrate tissue were set as 2.0 and 0.1 MPa, respectively. We further analyzed the effects of the thickness and gradient range of the gradient hydrogel on the stress distribution. The Young's modulus E of the gradient hydrogel at different radial positions is defined as:

$$E = E_0 + k \cdot R$$

where E_0 is the initial elastic modulus, k is the gradient coefficient, and R is the radius. The Young's modulus is linearly dependent on the radius.

Three-point bending simulations were conducted to compare the stress distributions. Coupling constraints were applied at reference points on both ends of the electrode, with ±30° rotational displacements about the y-axis imposed, whereas all the other degrees of freedom were constrained. Stress profiles were extracted along the neutral axis of the cross-section.

4.3 | Electrochemical Performance of RMGFs

The electrochemical performance of the RMGFs was evaluated using an electrochemical workstation (CHI660E, CH Instruments Ins.). An RMGF, platinum wire, and Ag/AgCl electrode were used as the working, counter, and reference electrodes, respectively. 1 × Phosphate-buffered saline (PBS) (pH = 7.4, Servicebio) was chosen as the electrolyte. For the impedance test, impedance spectroscopy was performed with a frequency sweep range of 1–100,000 Hz. The impedance parameters and impedance at 1.0 kHz were determined under the open-circuit voltage by using the impedance-time method.

To evaluate the electrochemical stability during dynamic deformation at different strain rates, one end of an RMGF was connected to a copper wire using silver glue, while the other end was exposed to the testing pool. The RMGF was fixed on a tensile machine (TA Instruments-Waters LLC ElectroForce 3220). Before measurement, 1 × PBS was added to the pool until the

exposed end of the RMGF was fully immersed. A platinum wire and a Ag/AgCl electrode were also immersed in 1 × PBS as the counter and reference electrodes, respectively. The RMGF was then stretched at 1.0% strain over a frequency sweep range of 0.1–10 Hz to assess the electrochemical stability. To further investigate the electrochemical stability under cyclic deformation, the RMGF was stretched at 1.0% strain and specific frequencies ranging from 0.1 to 10 Hz for 100 cycles.

4.4 | Electrical Performance of RMGFs

To investigate the electrical stability, an RMGF was fixed on a tensile machine (TA Instruments-Waters LLC ElectroForce 3220) with both ends connected to copper wires using silver glue. The electrical current was recorded at a voltage of 0.1 V using an electrochemical workstation with multiple potential parameters. The resistance was calculated according to Ohm's law. The RMGF was stretched at 1.0% strain over a frequency sweep range of 0.1–10 Hz to evaluate its electrical stability under different strain rates. Moreover, the RMGF was also stretched at different frequencies for 100 cycles and showed high stability under cyclic stretching. To further evaluate the electrical stability under large strains, the RMGF was tested on a tensile machine (HY0350) and stretched at a strain of 25% for 700,000 cycles at a tensile rate of 10 mm/s.

A 3-cm-long RMGF was bent with different curvature radii of 5, 10, 15, and 20 mm, as well as fully folded. At a curvature radius of 5 mm, the fibers were subjected to 5000 bending cycles. In addition, different weights were applied to the fibers. The electrical resistances of these fibers were measured using a digital multimeter.

4.5 | Animals

The animal experiments were approved by the Institutional Animal Care and Use Committee at Fudan University (protocol no. SYXK-Hu-2020-0032). Cats (weight of 2–3.5 kg, age of 0.5–2 years, randomized sex) were purchased from Shanghai Jiagan Biotechnology Co., Ltd. Mice (ICR, 6 weeks old, randomized sex) were purchased from Shanghai SLAC Laboratory Animal Co. Ltd. (certificate number: SYXK-Hu-2022-0012). All animals were housed in the animal care laboratory at the School of Life Sciences in accordance with the regulations set by the National Institutes of Health and Fudan University.

4.6 | Immunofluorescence Staining

After implantation of RMGFs into cat brains for 5 months, the brain tissue was fixed with 4% (v/v) paraformaldehyde for 24 h and sliced into approximately 3 μm-thick sections using a microtome (Leica RM 2135, Leica Microsystems). Immunofluorescence staining for glial fibrillary acidic protein (GFAP) and ionized calcium-binding adaptor molecule-1 (Iba-1) was performed to assess the inflammatory response caused by the implanted electrodes. The staining methods have been previously described in detail [46]. Fluorescence images were obtained using a microscope (Nikon C2+).

4.7 | Two-Photon Imaging

Thy1-YFP transgenic mice were used in this study. Electrodes were horizontally implanted into the brain tissue for subsequent experimental procedures. Electrode-inserted brain slices were imaged with a commercial two-photon microscope (DeepVision-2P, MicroLux Intelligent Co., Ltd., China) equipped with a 920 nm femtosecond pulsed laser (ALCOR 920–2, Spark Lasers). A specially designed optical system, with a 16 × water-immersion objective (CFI75 LWD 16X W, Nikon), provided a 1.6 mm × 1.6 mm field of view for both galvo scanning at 0.5 Hz and high-speed resonant scanning at 30 Hz. A near-axial, high-efficiency fluorescence detection path with a collection angle of up to 15° was used to maximize collection of both ballistic and scattered fluorescence utilizing high-sensitivity GaAsP photomultiplier tubes (H10770PA-40, Hamamatsu). Volume acquisition was performed with a scanning depth range of 200–400 μm and a plane interval of 5 μm by using a motorized objective stage. Each plane was captured at a resolution of 1024 × 1024 pixels. The laser power was dynamically adjusted within the range of 10–30 mW to optimize imaging at different depths.

4.8 | In Vivo Electrophysiological Recording

A 12-channel RMGF was fabricated by twisting together 12 fiber neural probes. The channels were spaced ~100 μm apart and connected to a flexible printed circuit board using silver glue, and the connection areas were encapsulated with silicone rubber. RMGFs were implanted into targeted brain regions of cats with the assistance of a commercial tungsten electrode bonded with a dissolvable gel (30 wt.%).

The cats were anesthetized with isoflurane (2.5%–4.0% (v/v) isoflurane in air). The head of the cat was held in place by ear bars, and its mouth gripped a salver to ensure that its eyes were positioned parallel to and facing the stimulation screen. Moreover, the rectal temperature was monitored and maintained at 38.5°C, and the exhaled CO_2 concentration was maintained at 3.8%. After removal of the hair and sterilization, an incision was made to expose the skull. The dorsal lateral geniculate nucleus (dLGN) was accurately located (Horsley-Clarke coordinates A6 and L9, 12–14 mm beneath the cortex surface). The skull and dura mater were carefully opened to expose the brain. RMGFs, glued with a commercial tungsten electrode by gelatin/physiological saline, were implanted into the dLGN. The exposed portion of the skull was immediately covered with a 4 wt.% agarose solution. The gel completely dissolved after 30 min in vivo, allowing the tungsten electrode to be withdrawn using a microcontroller at a controlled speed of 5 μm s^{-1}. Once this rigid electrode was completely removed, paraffin wax and dental cement were applied in turn to cover the agarose. Finally, the RMGFs and connectors were fixed on the skull for chronic recording in vivo.

During in vivo recording, the cats were anesthetized with 0.8–1.2% (v/v) isoflurane. The eyes of the cats were kept open and protected with hard contact lenses to ensure moisture, and their pupils were dilated with a drop of atropine. Various visual stimuli, including drifting grating stimuli to detect the cutoff spatial frequency, orientation bias (OB), and X/Y cells, light-dark screens to activate ON/OFF neurons, were used to excite the neurons.

For visual reconstruction, full-field oriented sinewave gratings (at their optimal spatial frequency and orientation) drifted at pseudorandom velocities, so that the drifting speed kept changing every 3 s.

4.9 | Visual Decoding In Vivo

The unscented Kalman filter (UKF) algorithm reconstructs the original visual stimuli from action potentials of the dLGN recorded by an RMGF. The state equation $\boldsymbol{x}_t$ and measurement equation $\boldsymbol{y}_t$ are shown in Equation (1):

$$\begin{cases} x_{t+1} = Ax_t + w_t \\ y_t = H(x_t) + n_t \end{cases} \tag{1}$$

Here, x_t represents the visual stimulus state, with $w_t \sim \mathcal{N}(0, Q)$ signifying the process noise in the stimulus dynamics. In our experiment $x_t \in \mathbb{R}$, and $Q \in \mathbb{R}$. The measurement y_t denotes the mean spike count over 100 trials at time t recorded using the RMGF. When using $m \in \{1, 2, 3\}$ cells, y_t is an m-dimensional vector and $H(\cdot)$ returns an m-dimensional output, and $n_t \sim \mathcal{N}(0, R)$, where n_t is the m-dimensional observation noise and $R \in \mathbb{R}^{m\times m}$ is its covariance. The state-transition parameter A is estimated by least-squares, while the nonlinear measurement mapping H is calculated by fitting a Volterra Kernel [47, 48].

The unscented transformation captures a nonlinear transformation [49]. For each time step t, we compute the sigma points χ from the state estimate:

$$\chi^{(0)}_{t-1|t-1} = \hat{x}_{t-1|t-1} \tag{2}$$

$$\chi^{(i)}_{t-1|t-1} = \hat{x}_{t-1|t-1} - \left(\sqrt{(L+\lambda)P_{t-1|t-1}}\right)_i,\ i = 1, \ldots, L \tag{3}$$

$$\chi^{(i)}_{t-1|t-1} = \hat{x}_{t-1|t-1} - \left(\sqrt{(L+\lambda)P_{t-1|t-1}}\right)_{i-L},\ i = L+1, \ldots, 2L \tag{4}$$

$$W^{(0)}_m = \lambda/(L+\lambda) \tag{5}$$

$$W^{(0)}_c = \frac{\lambda}{L+\lambda} + \left(1 - \alpha^2 + \beta\right) \tag{6}$$

$$W^{(i)}_m = W^{(i)}_c = \frac{1}{2(L+\lambda)},\ i = 1, 2, \ldots 2L \tag{7}$$

where i is the sigma-point index, λ is a scaling factor, with $\lambda = \alpha^2(L+\kappa) - L$, α determines the spread of sigma points around $\hat{x}_{t-1}$, and L is the number of states, κ is a secondary scaling parameter, $\sqrt{P}$ denotes a matrix square root, and $(\cdot)$ denotes its i-th column. In our case, $\alpha = 1\times10^{-3}$, $\beta = 2$, $\kappa = 0$, and $\hat{x}_0 = x_0$.

Each sigma point is propagated through the process model:

$$\chi^{(i)}_{t|t-1} = A\chi^{(i)}_{t-1|t-1} \tag{8}$$

The predicted state mean is computed by taking the weighted sum of the sigma points:

$$\hat{x}_{t|t-1} = \sum_{i=0}^{2L} W^{(i)}_m \chi^{(i)}_{t|t-1}. \tag{9}$$

The predicted covariance $P_{t|t-1}$ is computed by taking the weighted sum of the covariance of each sigma point:

$$P_{t|t-1} = \sum_{i=0}^{2L} W^{(i)}_c \left(\chi^{(i)}_{t|t-1} - \hat{x}_{t|t-1}\right)\left(\chi^{(i)}_{t|t-1} - \hat{x}_{t|t-1}\right)^T \tag{10}$$

Measurement prediction and update: Upon receiving a new measurement y_t, the update is calculated as follows:

$$\hat{y}^{(i)}_{t|t-1} = H\left(\chi^{(i)}_{t|t-1}\right),\ i = 0, \ldots, 2L \tag{11}$$

The predicted measurement mean $\hat{y}_{t|t-1}$ is computed:

$$\hat{y}_{t|t-1} = \sum_{i=0}^{2L} W^{(i)}_m \hat{y}^{(i)}_{t|t-1} \tag{12}$$

The predicted covariance P_{yy} and the cross-covariance P_{xy} are computed:

$$P_{yy} = \sum_{i=0}^{2L} W^{(i)}_c \left(\hat{y}^{(i)}_{t|t-1} - \hat{y}_{t|t-1}\right)\left(\hat{y}^{(i)}_{t|t-1} - \hat{y}_{t|t-1}\right)^T + R \tag{13}$$

$$P_{xy} = \sum_{i=0}^{2L} W^{(i)}_c \left(\chi^{(i)}_{t|t-1} - \hat{x}_{t|t-1}\right)\left(\hat{y}^{(i)}_{t|t-1} - \hat{y}_{t|t-1}\right)^T \tag{14}$$

The Kalman gain K_t is computed:

$$K_t = P_{xy}\, P^{-1}_{yy} \tag{15}$$

The state estimate is updated with the incoming measurement:

$$\hat{x}_t = \hat{x}_{t|t-1} + K_t\left(y_t - \hat{y}_{t|t-1}\right) \tag{16}$$

The state covariance is updated:

$$P_t = P_{t|t-1} - K_t P_{yy} K^T_t \tag{17}$$

4.10 | Reconstruction Quality

The Pearson correlation coefficient is employed to assess the relationship between the original and reconstructed stimuli over time. This correlation is calculated as follows:

$$r = \frac{\sum^n_{t=1}(x_t - \bar{x})\left(\hat{x}_t - \bar{\hat{x}}\right)}{\sqrt{\sum^n_{t=1}(x_t - \bar{x})^2}\sqrt{\sum^n_{t=1}\left(\hat{x}_t - \bar{\hat{x}}\right)^2}} \tag{18}$$

where x_t represents the observed data of the original visual stimulus at time t and $\hat{x}_t$ is the corresponding value of the reconstructed stimulus obtained by the UKF algorithm. $\bar{x}$ is the

mean of the original stimulus, $\bar{\hat{x}}$ is the mean of the reconstructed stimulus, and n is the total number of time steps.

4.11 | Stimulus-Response Latency

To determine the latency between the original stimulus $x[t]$ and the reconstructed stimulus $\hat{x}[t]$, the cross-correlation $R_{x\hat{x}}[\tau]$ is computed. The cross-correlation function is calculated as follows:

$$R_{x\hat{x}}\ [\tau] = \sum_{t} x\,[t]\ \cdot \hat{x}\,[t+\tau] \tag{19}$$

where $\hat{x}[t+\tau]$ represents the value of the reconstructed stimulus at time $t+\tau$ and τ is the time lag variable. The lag τ at which $R_{x\hat{x}}[\tau]$ is maximized indicates the estimated latency between the original and reconstructed stimuli.

4.12 | Statistical Analysis

Statistical analysis was performed with Graphpad Prism 9.0 and Origin 2018. The results are expressed as mean ± s.d. The statistical differences between the two groups were analyzed using an unpaired two-tailed t-test. p values: n.s., not significant ($p > 0.05$), $^{*}p < 0.05$, $^{**}p < 0.01$, $^{***}p < 0.005$, and $^{****}p < 0.001$.

Acknowledgements

We thank Yao Wu from MicroLux (Shanghai) Intelligent Science & Technology Co., Ltd. for their contribution to two-photon imaging data acquisition. We thank Jiapeng Xu of the Department of Applied Mathematics, The Hong Kong Polytechnic University (Hong Kong, China) for the support with the visual reconstruction. This work was supported by NSFC (Nos. T2321003, 22335003, 52222310, T2222005, 32371047, 31970928, 52473208, 52203256, U20A20221, and 12502061), MOST (Nos. 2022YFA1203001 and 2022YFA1203002), Scientific Research Innovation Capability Support Project for Young Faculty (No. ZYGXQNJSKYCXNLZCXM-M7), SMCST (No. 25CL2900505), SMST project (No. 2018SHZDZX01), NSFC-SH (No. 24ZR1404300), STI2030-BS (2021ZD0201301), NK-RD Program (No. 2022YFF0708700), CPSF (No. 2023M740652), and ZJLab (H.Y.).

Conflicts of Interest

Biqin Dong is a founder and equity holder of MicroLux (Shanghai) Intelligent Science & Technology Co., Ltd. and Lishi Intelligent Science & Technology (Shanghai) Co., Ltd. The authors declare that they have no competing interests.

Data Availability Statement

The data that support the findings of this study are available in the supplementary material of this article.

References

1. D. Lyu, J. R. Stiger, Z. Lusk, V. Buch, and J. Parvizi, "Mapping Human Thalamocortical Connectivity with Electrical Stimulation and Recording," *Nature Neuroscience* 28 (2025): 1797–1809, https://doi.org/10.1038/s41593-025-02009-x.

2. S. Segobin, R. A. M. Haast, V. J. Kumar, et al., "A Roadmap towards Standardized Neuroimaging Approaches for Human Thalamic Nuclei," *Nature Reviews Neuroscience* 25 (2024): 792–808, https://doi.org/10.1038/s41583-024-00867-1.

3. W. Shi, A. Xianyu, Z. Han, et al., "Ontogenetic Establishment of Order-Specific Nuclear Organization in the Mammalian Thalamus," *Nature Neuroscience* 20 (2017): 516–528, https://doi.org/10.1038/nn.4519.

4. J. M. Shine, L. D. Lewis, D. D. Garrett, and K. Hwang, "The Impact of the Human Thalamus on Brain-Wide Information Processing," *Nature Reviews Neuroscience* 24 (2023): 416–430, https://doi.org/10.1038/s41583-023-00701-0.

5. S. Zhao, G. Li, C. Tong, et al., "Full Activation Pattern Mapping by Simultaneous Deep Brain Stimulation and fMRI with Graphene Fiber Electrodes," *Nature Communications* 11 (2020): 1788, https://doi.org/10.1038/s41467-020-15570-9.

6. A. Sahasrabudhe and P. Anikeeva, "Wireless Microelectronic Fibers to Discover Gut and Brain Pathways," *Nature Biotechnology* 42 (2024): 852–853, https://doi.org/10.1038/s41587-023-01850-4.

7. S. Park, Y. Guo, X. Jia, et al., "One-Step Optogenetics with Multifunctional Flexible Polymer Fibers," *Nature Neuroscience* 20 (2017): 612–619, https://doi.org/10.1038/nn.4510.

8. J. A. Frank, M. J. Antonini, and P. Anikeeva, "Next-Generation Interfaces for Studying Neural Function," *Nature Biotechnology* 37 (2019): 1013–1023, https://doi.org/10.1038/s41587-019-0198-8.

9. S. Lv, Z. Xu, F. Mo, et al., "Long-Term Stability Strategies of Deep Brain Flexible Neural Interface," *npj Flexible Electronics* 9 (2025): 40, https://doi.org/10.1038/s41528-025-00410-x.

10. J. Jaepel, M. H, T. Bonhoeffer, and T. Rose, "Lateral Geniculate Neurons Projecting to Primary Visual Cortex Show Ocular Dominance Plasticity in Adult Mice," *Nature Neuroscience* 20 (2017): 1708–1714, https://doi.org/10.1038/s41593-017-0021-0.

11. Y. Cho, S. Park, J. Lee, and K. J. Yu, "Emerging Materials and Technologies with Applications in Flexible Neural Implants: a Comprehensive Review of Current Issues with Neural Devices," *Advanced Materials* 33 (2021): 2005786, https://doi.org/10.1002/adma.202005786.

12. A. K. Knutsen, A. D. Gomez, M. Gangolli, et al., "In Vivo Estimates of Axonal Stretch and 3D Brain Deformation during Mild Head Impact," *Brain Multiphysics* 1, no. 1 (2020): 100015, https://doi.org/10.1016/j.brain.2020.100015.

13. J. J. Sloots, G. J. Biessels, and J. J. M. Zwanenburg, "Cardiac and Respiration-Induced Brain Deformations in Humans Quantified with High-Field MRI," *Neuroimage* 210 (2020): 116581, https://doi.org/10.1016/j.neuroimage.2020.116581.

14. A. Canales, X. Jia, U. P. Froriep, et al., "Multifunctional Fibers for Simultaneous Optical, Electrical and Chemical Interrogation of Neural Circuits in Vivo," *Nature Biotechnology* 33 (2015): 277–284, https://doi.org/10.1038/nbt.3093.

15. J. J. Jun, N. A. Steinmetz, J. H. Siegle, et al., "Fully Integrated Silicon Probes for High-Density Recording of Neural Activity," *Nature* 551 (2017): 232–236, https://doi.org/10.1038/nature24636.

16. T. D. Y. Kozai, N. B. Langhals, P. R. Patel, et al., "Ultrasmall Implantable Composite Microelectrodes with Bioactive Surfaces for Chronic Neural Interfaces," *Nature Materials* 11 (2012): 1065–1073, https://doi.org/10.1038/nmat3468.

17. L. Lu, X. Fu, Y. Liew, et al., "Soft and MRI Compatible Neural Electrodes from Carbon Nanotube Fibers," *Nano Letters* 19 (2019): 1577–1586, https://doi.org/10.1021/acs.nanolett.8b04456.

18. N. A. Steinmetz, C. Aydin, A. Lebedeva, et al., "Neuropixels 2.0: a Miniaturized High-Density Probe for Stable, Long-Term Brain Recordings," *Science* 372 (2021): abf4588, https://doi.org/10.1126/science.abf4588.

19. S. Park, H. Yuk, R. Zhao, et al., "Adaptive and Multifunctional Hydrogel Hybrid Probes for Long-Term Sensing and Modulation of Neural Activity," *Nature Communications* 12 (2021): 3435, https://doi.org/10.1038/s41467-021-23802-9.

20. A. C. Paulk, Y. Kfir, A. R. Khanna, et al., "Large-Scale Neural Recordings with Single Neuron Resolution Using Neuropixels Probes in Human Cortex," *Nature Neuroscience* 25 (2022): 252–263, https://doi.org/10.1038/s41593-021-00997-0.

21. W. M. Han, S.-J. Heo, T. P. Driscoll, et al., "Microstructural Heterogeneity Directs Micromechanics and Mechanobiology in Native and Engineered Fibrocartilage," *Nature Materials* 15 (2016): 477–484, https://doi.org/10.1038/nmat4520.

22. M. Wang, K. Wang, C. Ma, P. C. Uzabakiriho, X. Chen, and G. Zhao, "Mechanical Gradients Enable Highly Stretchable Electronics Based on Nanofiber Substrates," *ACS Applied Materials & Interfaces* 14 (2022): 35997–36006, https://doi.org/10.1021/acsami.2c10245.

23. A. J. Boys, J. A. M. R. Kunitake, C. R. Henak, I. Cohen, L. A. Estroff, and L. J. Bonassar, "Understanding the Stiff-to-Compliant Transition of the Meniscal Attachments by Spatial Correlation of Composition, Structure, and Mechanics," *ACS Applied Materials & Interfaces* 11 (2019): 26559–26570, https://doi.org/10.1021/acsami.9b03595.

24. S. Gharazi, B. C. Zarket, K. C. DeMella, and S. R. Raghavan, "Nature-Inspired Hydrogels with Soft and Stiff Zones That Exhibit a 100-Fold Difference in Elastic Modulus," *ACS Applied Materials & Interfaces* 10 (2018): 34664–34673, https://doi.org/10.1021/acsami.8b14126.

25. S. Xin, J. Dai, C. A. Gregory, A. Han, and D. L. Alge, "Creating Physicochemical Gradients in Modular Microporous Annealed Particle Hydrogels via a Microfluidic Method," *Advanced Functional Materials* 30 (2020): 1907102, https://doi.org/10.1002/adfm.201907102.

26. C. Li, et al., "Buoyancy-Driven Gradients for Biomaterial Fabrication and Tissue Engineering," *Advanced Materials* 31 (2019): 1900291, https://doi.org/10.1002/adma.201900291.

27. H. Yuk, B. Lu, and X. Zhao, "Hydrogel Bioelectronics," *Chemical Society Reviews* 48 (2019): 1642–1667, https://doi.org/10.1039/c8cs00595h.

28. H. Yuk, J. W, and X. Zhao, "Hydrogel Interfaces for Merging Humans and Machines," *Nature Reviews Materials* 7 (2022): 935–952, https://doi.org/10.1038/s41578-022-00483-4.

29. X. Xue, et al., "Fabrication of Physical and Chemical Crosslinked Hydrogels for Bone Tissue Engineering," *Bioactive Materials* 12 (2022): 327–339, https://doi.org/10.1016/j.bioactmat.2021.10.029.

30. A. Gautam and P. K, "Synthesis of Montmorillonite Clay/Poly (vinyl alcohol) Nanocomposites and Their Mechanical Properties," *Journal of Nanoscience and Nanotechnology* 19 (2019): 8071–8077, https://doi.org/10.1166/jnn.2019.16869.

31. S. Lin, X. Liu, J. Liu, et al., "Anti-Fatigue-Fracture Hydrogels," *Science Advances* 5 (2019): aau8528, https://doi.org/10.1126/sciadv.aau8528.

32. K. Shirasu, G. Yamamoto, I. Tamaki, et al., "Negative Axial Thermal Expansion Coefficient of Carbon Nanotubes: Experimental Determination Based on Measurements of Coefficient of Thermal Expansion for Aligned Carbon Nanotube Reinforced Epoxy Composites," *Carbon* 95 (2015): 904–909, https://doi.org/10.1016/j.carbon.2015.09.026.

33. K. Shirasu, A. Nakamura, G. Yamamoto, et al., "Potential Use of CNTs for Production of Zero Thermal Expansion Coefficient Composite Materials: an Experimental Evaluation of Axial Thermal Expansion Coefficient of CNTs Using a Combination of Thermal Expansion and Uniaxial Tensile Tests," *Composites Part A: Applied Science and Manufacturing* 95 (2017): 152–160, https://doi.org/10.1016/j.compositesa.2016.12.027.

34. J. Ortigoza-Diaz, K. Scholten, C. Larson, et al., "Techniques and Considerations in the Microfabrication of Parylene C Microelectromechanical Systems," *Micromachines* 9 (2018): 422, https://doi.org/10.3390/mi9090422.

35. A. A. Sitko and L. V. Goodrich, "Making Sense of Neural Development by Comparing Wiring Strategies for Seeing and Hearing," *Science* 371 (2021): 140, https://doi.org/10.1126/science.aaz6317.

36. J. Jin, Y. Wang, H. A. Swadlow, and J. M. Alonso, "Population Receptive Fields of ON and OFF Thalamic Inputs to an Orientation Column in Visual Cortex," *Nature Neuroscience* 14 (2011): 232–238, https://doi.org/10.1038/nn.2729.

37. T. D. Shou and A. G. Leventhal, "Organized Arrangement of Orientation-Sensitive Relay Cells in the Cat's Dorsal Lateral Geniculate Nucleus," *The Journal of Neuroscience* 9 (1989): 4287–4302, https://doi.org/10.1523/JNEUROSCI.09-12-04287.1989.

38. S. B. Rompani, F. E. Müllner, A. Wanner, et al., "Different Modes of Visual Integration in the Lateral Geniculate Nucleus Revealed by Single-Cell-Initiated Transsynaptic Tracing," *Neuron* 93 (2017): 1519, https://doi.org/10.1016/j.neuron.2017.03.009.

39. R. Shapley, E. Kaplan, and R. Soodak, "Spatial Summation and Contrast Sensitivity of X and Y Cells in the Lateral Geniculate Nucleus of the Macaque," *Nature* 292 (1981): 543–545, https://doi.org/10.1038/292543a0.

40. M. Schneider, A. C. Broggini, B. Dann, et al., "A Mechanism for Inter-Areal Coherence through Communication Based on Connectivity and Oscillatory Power," *Neuron* 109 (2021): 4050–4067.e12, https://doi.org/10.1016/j.neuron.2021.09.037.

41. J. H. Siegle, X. Jia, S. Durand, et al., "Survey of Spiking in the Mouse Visual System Reveals Functional Hierarchy," *Nature* 592 (2021): 86–92, https://doi.org/10.1038/s41586-020-03171-x.

42. G. B. Stanley, F. F. Li, and Y. Dan, "Reconstruction of Natural Scenes from Ensemble Responses in the Lateral Geniculate Nucleus," *The Journal of Neuroscience* 19 (1999): 8036–8042, https://doi.org/10.1523/JNEUROSCI.19-18-08036.1999.

43. S. Tang, Y. Zhang, Z. Li, et al., "Large-Scale Two-Photon Imaging Revealed Super-Sparse Population Codes in the V1 Superficial Layer of Awake Monkeys," *Elife* 7 (2018): 33370, https://doi.org/10.7554/eLife.33370.

44. M. Wang, X. Liao, R. Li, et al., "Single-neuron Representation of Learned Complex Sounds in the Auditory Cortex," *Nature Communications* 11 (2020): 4361, https://doi.org/10.1038/s41467-020-18142-z.

45. L. Wang, F. Wan, Y. Xu, et al., "Hierarchical Helical Carbon Nanotube Fibre as a Bone-Integrating Anterior Cruciate Ligament Replacement," *Nature Nanotechnology* 18 (2023): 1085–1093, https://doi.org/10.1038/s41565-023-01394-3.

46. J. Wang, L. Wang, Y. Yang, et al., "A Fiber Sensor for Long-Term Monitoring of Extracellular Potassium Ion Fluctuations in Chronic Neuropsychiatric Diseases," *Advanced Materials* 36 (2024): 2309862, https://doi.org/10.1002/adma.202309862.

47. R. Kelly and T. S. Lee, "Decoding V1 Neuronal Activity Using Particle Filtering with Volterra Kernels," *Advances in Neural Information Processing Systems* 16 (2003): 1359–1366.

48. W. Wu, M. Black, Y. Gao, et al., "Neural Decoding of Cursor Motion Using a Kalman Filter," *Advances in Neural Information Processing Systems* 15 (2002): 133–140.

49. E. A. Wan and R. Van Der Merwe, "The Unscented Kalman Filter for Nonlinear Estimation," in Proceedings of the IEEE Adaptive Syst Signal Process Commun Control Symp (IEEE, 2000): 153–158, https://doi.org/10.1109/ASSPCC.2000.882463.

Supporting Information

Additional supporting information can be found online in the Supporting Information section.

Supporting File: adma73099-sup-0001-SuppMat.docx.